where $g(P_m)$ is expressed in degrees and P_m in thousandths. *Dollfus and Bowell* (1971) note that uniform behavior of polarization across the entire observable lunar disk provides strong evidence that the properties of the microstructure of the upper lunar surface are remarkably uniform all across the Moon.

A fascinating correlation between the polarization maximum (P_m) and the normal albedo (A) has also been discovered. The relation is given by

$$\log A = -(0.724 \pm 0.005)\log P_m - (1.81 \pm 0.02)$$

A similar relationship between geometric albedo (q) and the slope of the polarization curve at the inversion point has also been documented in later work (*Zellner et al.,* 1977). This latter correlation has proved to be particularly important in the determination of albedos of asteroids and other small bodies in the solar system. Based on both lunar sample measurements and lunar observations (*Bowell et al.,* 1973), the best-fit relation for the Moon is

$$\log p = -1.04 \log h - 1.88$$

where p is the geometric albedo for a lunar region and h is the inversion slope given in percent per degree. This relation is also consistent with one derived by *Veverka and Noland* (1973) from lunar data published by *Dollfus and Bowell* (1971) and *Dollfus et al.* (1971).

9.3.2. Radar Astronomy

Powerful radar installations built for military purposes during World War II were subsequently utilized in the postwar period to detect echoes reflected from the Moon. The first successful attempts in 1946 produced only marginal returned signals (*DeWitt and Stodola,* 1949), but rapid improvements in the technology soon made possible accurate ranging to the Moon, measurements of the Doppler shifts produced by lunar motions, the detection of Faraday rotation of the polarization vector of the signals in the Earth's ionosphere, the determination of the gross radar scattering law for the lunar surface, and estimates of the Moon's radar cross-section (*Evans,* 1962).

The transmitted radio signal can be pictured as a plane wave traveling from the antenna and striking the Moon. If the Moon behaves like a smooth dielectric sphere, the plane wave will strike it first at the point closest to the antenna—the *subradar point.* The only energy reflected back to the antenna would come from a small zone surrounding the subradar point, corresponding to the area of the first Fresnel zone of the wavefront. The remainder of the incoming energy would be scattered by the rest of the Moon and would travel in other directions, according to the laws of specular reflection.

Most of the returned energy is observed to come from an area surrounding the subradar point. However, definite radar echoes can be detected from regions out to the lunar limb, implying that the lunar surface is not entirely smooth at radar wavelengths. For these reasons, radar reflection from the Moon is commonly described as "quasispecular," because the strong central reflection only approximates the expected behavior of an ideally smooth spherical mirror.

Radar backscattering. The brightness (*cross-section*) of the subradar point is a measure of the dielectric constant of the lunar surface, while the shape of the trailing echo (*scattering function*) is a measure of the surface roughness and heterogeneity of the surface on the scale of the wavelength being used. The radar echo from the zone immediately around the subradar point is approximately three orders of magnitude stronger than the echo from the annular region at the lunar limb (*Thompson,* 1979).

Radar systems have the capability to transmit energy with a single mode of polarization and then to detect and analyze the returned energy in both the originally transmitted mode of polarization and the orthogonal mode. Commonly the transmitted signal is circularly polarized to minimize the effects of Faraday rotation during the signal's outward passage through the Earth's ionosphere. The process of reflection from an ideal dielectric sphere reverses the direction of circular polarization. When lunar radar observations are made, the energy returned with the direction of polarization to be expected from an ideal sphere is called *polarized*; the energy received in the other direction of polarization is called *depolarized.* A nonspecular component is also present in the polarized return; this component is qualitatively attributed to flat surfaces that happen to be tilted toward the radar. The depolarized return is attributed to the presence of surface rocks and surface roughness. Radar energy can penetrate a distance of 10 to 50 wavelengths into the extremely dry lunar regolith, allowing subsurface rocks, possibly as deep as several meters, to contribute to the radar reflections returned to Earth.

Although the strengths of the polarized and depolarized returns (echoes) are quite different near the subradar point, the falloff in the strengths of the two types of returns toward the limb regions exhibits somewhat similar behavior (*Hagfors,* 1967). Near the subradar point, the polarized echoes are quite strong, and they decrease sharply and nonuniformly with increasing angle of incidence from the subradar point ($i = 0°$) outward to about $i = 35°$. From about $i = 35°$ outward, the slope of the angular dependence becomes more gradual, varying as $\cos^{3/2} i$ out to approximately $i = 80°$ (*Evans and Hagfors,* 1966). Beyond $i = 80°$ to the limb ($i = 90°$), the dependence is proportional to $\cos i$. In contrast, the strength of the depolarized echo varies uniformly as $\cos i$ from the subradar point outward.

Although the lunar radar backscattering law is similar in form at all wavelengths, the fraction of power in the diffusely scattered component varies considerably, being much greater at higher frequencies (*Hagfors,* 1970). As a result, the lunar disk appears more uniformly bright when illuminated by the shorter radar wavelengths. Pettengill (discussion following *Hagfors,* 1970) points out that a plot comparing the lunar scattering laws is misleading when the plots are normalized to unity at the subradar point. Rather, it is more meaningful to scale the areas of the curves to be proportional to the total radar cross-sections at the corresponding wavelengths.

The form of the scattering law that is most widely used for studying the Moon and the inner planets is (*Ostro,* 1983)

$$\sigma_o(\phi) = 0.5\, \rho \beta^2_{rms} \times (\cos^4\phi + \beta^{-2}_{rms} \sin^2\phi)^{-3/2}$$

where σ_o is radar cross-section per unit area, ϕ is the angle of incidence, ρ is the Fresnel normal-incidence power reflection, and β_{rms} is the root-mean-square surface slope at wavelength-dependent scales. The theoretical basis for this model can be found in *Hagfors* (1964, 1970).

Radar cross-section. To understand the radar signal returned from the Moon, we use the basic radar equation that says

Received Power =
Transmitted Power Density at the Moon ×
Backscatter Cross-Section of the Moon ×
Geometrical Attenuation on Return Path ×
Effective Antenna Aperture

For a transmitter of power P_t, the power density at the distance of the Moon, R, is given by $P_t G/4\pi R^2$. The denominator of this expression is just the geometrical attenuation due to the familiar inverse-square law, and the antenna gain G can be related to the effective antenna aperture A by

$$G = 4\pi A/\lambda^2$$

where λ is the wavelength of observation. Combining these terms, we get an expression for received echo power P_r (*Ostro,* 1983)

$$P_r = P_t \frac{G^2\lambda^2}{(4\pi)^3 R^4} \sigma$$

where σ is the radar cross-section of the Moon.

The radar *cross-section* σ has the dimensions of an area and is defined as the geometrical cross-section of a metallic sphere whose radar echo has the same strength as the Moon. We can relate this quantity to the physical parameters of the Moon by considering the Moon as an absorbing dielectric sphere of radius a. Following a derivation presented by *Bohren and Huffman* (1983, p. 120), we can write

$$\sigma/\pi a^2 = g\rho$$

where ρ is the Fresnel reflection coefficient of the dielectric material (*Evans and Hagfors,* 1964) and g is a gain factor equal to unity for our ideal sphere. Because the Moon is not ideally smooth, some of the returned signal comes from reflections outside the small region surrounding the subradar point. (This is the *diffuse component* of the polarized return.) Because the lunar surface is not perfectly absorbing, some of the returned echo comes from scattering within the surface. (This is the *depolarized component.*) For these reasons, g is larger than unity by some unknown amount.

The product $g\rho$ can be derived directly from observational data. If the gain factor can be independantly calculated, then the dielectric constant (ϵ) of the lunar surface can be obtained from the relation

$$\rho = \frac{\sqrt{(\epsilon - 1)}}{\sqrt{(\epsilon + 1)}}$$

Attempts to calculate (*Rea et al.,* 1964, 1965) or estimate (*Evans and Hagfors,* 1964) the gain factor have resulted in estimates of the dielectric constant, ϵ, given by *Hagfors* (1970). Further complications can be introduced into these calculations by assuming that the surface consists of layers with differing dielectric properties or that the dielectric properties vary smoothly with depth in some way (*Hagfors,* 1970), both of which assumptions are more apt to be more realistic representations of the actual lunar surface.

Bistatic radar observations. When spacecraft were placed into orbit about the Moon, it became possible to carry out *bistatic radar* experiments in which the transmitting and receiving antennas are in different places. In the lunar experiments, antennas on Earth could detect both the direct radio or radar transmissions from the spacecraft and the nearly simultaneous reflections of the signals from the lunar surface toward Earth. A small Doppler shift in the reflection wavelength relative to the transmission wavelength allows the two signals to be differentiated. The orbital motion of the radar-

sounding spacecraft causes the point of specular reflection to move across the lunar surface along the ground track. Careful measurement of the intensity and polarization of the returned signals yields information on the reflectivity of the lunar material, possible subsurface layering, and surface slopes (*Tyler,* 1968b).

The effective surface resolution element in these experiments corresponds to the first Fresnel zone associated with the quasispecular reflection. The size of this zone depends on the altitude of the spacecraft as well as on the surface slope distribution. For measurements made using Explorer 35 in 1967, the surface resolution was approximately 100 km (*Tyler,* 1968a). For the Apollo 14 and 15 experiments, the resolution elements varied from 10 to 40 km, depending on the nature of terrain overflown (*Tyler and Howard,* 1973).

During a pass over Oceanus Procellarum, the transmitted signal from Explorer 35 was maintained with its linear polarization lying approximately in the plane of incidence. A Brewster null in the reflected signal was observed at an angle of incidence of $60° \pm 1°$, a result corresponding to a dielectric constant of 3.0 ± 0.2 at a wavelength of 2.2 m (*Tyler,* 1968a). This measurement was made in mare material located north-northwest of Hansteen Crater, and the result corresponds to the dielectric properties of the surface material averaged over a depth of roughly $\lambda/8$ (25 cm). The reflectivity along groundtracks in Oceanus Procellarum showed quite reproducible enhancements of approximately 30% in echo intensity for mare regions compared to highland areas (*Tyler,* 1968b). These differences in reflectivity can be explained either by variations in the packing fraction of the regolith or by variations in its depth. The latter explanation appears more physically realistic if one also takes into account the results of Earth-based observations.

The Apollo 14 and 15 missions provided the opportunity to continue bistatic radar investigations at wavelengths of 13 cm and 116 cm (*Tyler and Howard,* 1973). The signal-to-noise ratio and the surface resolution of these measurements were both an order of magnitude better than previous experiments of the same type. Although the extent of the datasets obtained was limited, the investigators found regions of the lunar surface whose physical properties could not easily be explained by simple models.

For $\lambda = 13$ cm, mare surfaces could be modeled well using a value of the dielectric constant $\epsilon = 3.1$, with few deviations observed. At $\lambda = 116$ cm, much of the mare could also be modeled simply with a similar dielectric constant, but in this case, considerable deviations from the simple characterization were observed. No successful models for the structure and properties of the anomalous regions could be developed; the authors speculated that their data implied the existence of some frequency dispersive mechanism, such as layering in a high-loss dielectric medium.

In highland regions the longer wavelength (116 cm) data were fitted successfully to a model using a uniform dielectric interface with $\epsilon = 2.8$, a lower value for dielectric constant than that found in the maria. Observations at the shorter wavelength (13 cm) in the Apennine Mountains and in the central highland regions also yielded consistent results, but the data from units in the Palus Somni area and the rim of Mare Crisium could not be fitted with simple models at $\lambda = 13$ cm.

Since the polarization of returned radio signals can be determined, the echoes from the lunar surface also contain information about slopes and surface roughness. The complexity of both the surface and the physical mechanisms that alter the polarization of the signal permit only some general statements with any degree of confidence. In general, slopes in the highlands are higher than slopes in the maria. At $\lambda = 13$ cm, highland rms (root-mean-square) slopes range from 6° to 8°, while mare rms slopes range from 2° to 4° (*Tyler and Howard,* 1973). Although values derived from the 116-cm observations agree with the 13-cm data in the highlands, the mare values are only half as large as those derived from the 13-cm data. Apparently, small-scale roughness is larger in the maria.

Little work has yet been done on the lunar surface itself to verify the surface structures inferred from radar scattering behavior. A more technical discussion of these issues is found in *Tyler* (1979).

Apollo Lunar Sounder Experiment (ALSE). The ALSE was a three-channel, synthetic-aperture, orbital radar experiment operated during three orbits of the Apollo 17 mission to infer subsurface electrical conductivity structure, to profile lunar surface topographic variations, and to image the surface along the spacecraft ground track (*Phillips et al.,* 1973a,b). In this experiment, a continuous series of short bursts of radar energy at three frequencies (5, 15, and 150 MHz) was directed from an instrument on the spacecraft toward the lunar surface, and the reflections, received by the same instrument, were measured in terms of intensity, time of arrival, and phase. The very low electrical loss characteristics of the lunar regolith permitted detection of echoes from subsurface features as well as from the surface itself.

Reduction of the ALSE data has been a very complex process, and analysis of the information has been hampered by two fundamental problems (*Sharpton et al.,* 1984). First, the relatively weak signals returned from subsurface reflectors are obscured by strong surface clutter. Second, time delays associated with signals from subsurface features cannot be unambiguously distinguished from those associated with surface features lying some distance from the ground track. These problems have been overcome to some extent in the data from flat mare regions by correlating reflections from adjacent ground tracks. This correlation allows discrimination between subsurface layers and long linear surface features, which coincidentally parallel the orbital path and produce reflections at a distance from it (*Peeples et al.,* 1978).

Thus far, reflecting subsurface layers have been detected with confidence in both Mare Serenitatis and Mare Crisium. The placement and extent of the reflectors beneath Mare Serenitatis have been used to infer the geological history of the basin (see Fig. 4.31) (*Maxwell,* 1978; *Sharpton and Head,* 1982), illustrating the potential of the information in the ALSE dataset.

Range data from the ALSE was used (*W. E. Brown et al.,* 1974) to produce continuous elevation profiles around the Moon. These profiles, which extended along nearly two complete lunar orbits, were constructed from sampling at intervals of about

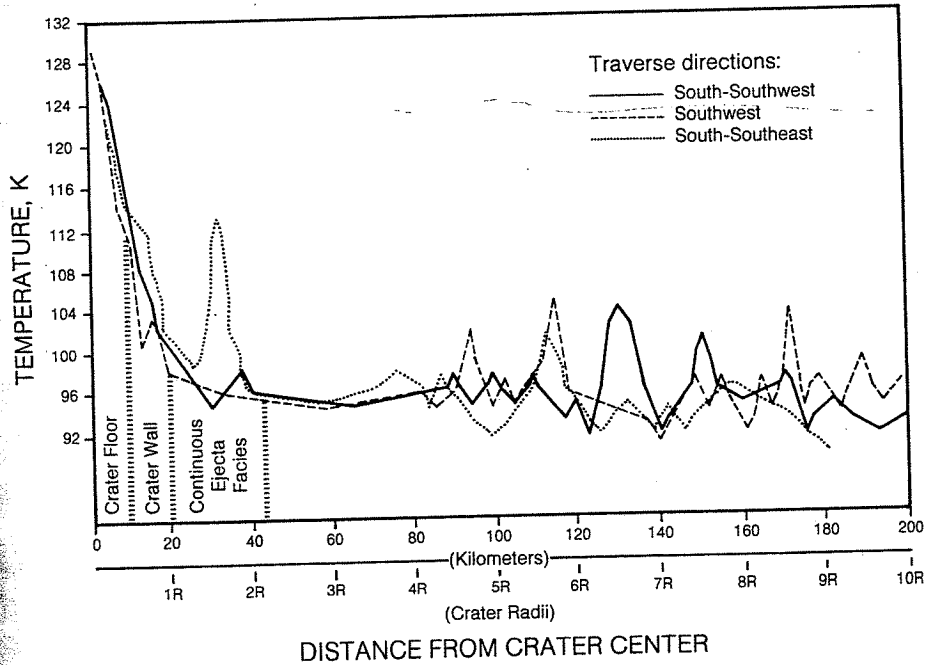

Fig. 9.77. Temperature profiles across Aristarchus Crater, a large central-peak crater emplaced in a mare region. Temperatures were determined from Earth-based thermal infrared measurements. Profiles originate at the center of the crater and traverse the crater in the directions indicated (southwest, south-southwest, and south-southeast). The higher pre-sunrise temperatures of the center indicate that much of the crater interior consists of large blocks of exposed bedrock. The nighttime temperatures fall significantly along the crater floor and are low but somewhat variable across the skirt of continuous ejecta around the crater. The ejecta deposits that occur beyond the limit of near-crater continuous ejecta and as far out as three crater radii (60 km) from the rim have smooth and uniform temperature profiles, unlike the irregular mare surface that is exposed beyond the ejecta. From *Schultz and Mendell* (1978).

45 m along the orbital ground tracks. *Elachi et al.* (1976) later used these elevation profiles to derive diameter/depth ratios for small craters along the flight path and to study the topography of a few large craters. They also published very accurate (better than ±25 m in elevation) profiles of Mare Crisium and Mare Serenitatis.

9.3.3. Thermal Infrared Astronomy

The emission of thermal IR ($\lambda = 3$–$15\ \mu m$) radiation from the darkened Moon provides information on heat retention as the lunar surface cools during the two-week-long lunar night. An IR scanning radiometer was operated in the orbiting command module during the Apollo 17 mission. This instrument collected data on lunar surface emissions in the wavelength range from 1.2 μm to about 70 μm. The Apollo 17 instrument was capable of resolution on the scale of a 2.2-km-diameter circle on the surface immediately beneath the spacecraft. However, since the collecting mirror on the instrument rotated at right angles to the flight path, the resolvable area degenerated into an ellipse toward the lateral horizons (*Mendell and Low,* 1975). The useful scanned area was within a band of ±6° of the command module's orbital latitude. Compared to IR observations made from Earth, which have lunar surface resolutions no better than 20 km and also suffer from atmospheric interference, the Apollo 17 data are an order of magnitude better (*Low and Mendell,* 1973).

The lunar nighttime surface temperature falls from about 100 K at the antisolar meridian to about 90 K at the sunrise terminator. Superimposed on this general nighttime cooling, however, are many "hot spots" that cool more slowly and therefore retain more of their heat during the lunar night. There is a strong correlation between the locations of these hot spots and the interiors of fresh craters, where large blocks are exposed (*Mendell,* 1976). In a pulverized regolith, composed of small particles and having a large ratio of surface area to particle mass, absorbed heat is lost more rapidly than from large blocks or from outcrops with a small ratio of surface area to mass. *Winter* (1970) showed that rocks smaller than 30 cm tend to have thermal losses just like soil, but rocks larger than 10 m retain heat as if they were solid outcrop.

The most significant result from the Apollo 17 IR radiometer is that its data can be used to provide estimates of minimum large-block sizes and abundances in the centers of young craters. In Aristarchus Crater, for example, the temperature in the crater center just a few hours before sunrise is as high as 120–130 K, whereas the crater walls and the surrounding plains are about 100 K (Fig. 9.77; *Mendell,* 1976; *Schultz and Mendell,* 1978). The thermal retention in Aristarchus is too great to be modeled, even by 3-m blocks, and the thermal behavior is more consistent with a model in which about 11% to 16% of the crater interior is outcrop. Similar extreme temperature differences were recorded in the central peak area of Copernicus Crater. In addition, some smaller fresh craters have heat-retentive rims (e.g., Bessarion A and B Craters; *Mendell and Low,* 1975). Both these central and marginal thermal anomalies disappear in older craters, and this loss of large blocky exposures or outcrops that retain heat can be used as another measure of crater age (see Chapters 4 and 10).

Thermal IR mapping may be a practical method for locating lunar outcrops of large blocks or solid rock. These data would supplement the information on mineralogic composition that would be obtained from shorter wavelength near-IR spectroscopy (Chapter 10).

APPENDIX: SUPPLEMENTARY DATA ON LUNAR PHYSICAL PROPERTIES (Tables A9.1–A9.16; Figs. A9.1–A9.9)

TABLE A9.1. Particle size distributions of Apollo 17 soils (after *McKay et al.,* 1974), with graphical size parameters (after *Folk and Ward,* 1957); (1) <1-cm data, (2) <1-mm data only.

		Median Grain Size		Graphic Mean		Inclusive Graphic Standard Deviation	Inclusive Graphic Skewness	Graphic Kurtosis
Sample		$M_d\ \phi$	$M_d\ \mu m$	$M_z\ \phi$	$M_z\ \mu m$	$\sigma_1\phi$	SK_1	K_0
1. 70161,1	(1)	3.91	66.5	3.89	67.5	2.03	−0.06	1.06
	(2)	4.01	62.1	4.08	59.1	1.76	−0.06	0.92
2. 70181,1	(1)	3.93	65.6	3.91	66.5	2.07	−0.08	1.07
	(2)	4.10	58.3	4.12	57.5	1.74	+0.03	0.88
3. 71041,1	(1)	3.58	83.6	3.13	114.2	2.92	−0.27	1.20
	(2)	4.08	59.1	4.15	56.3	1.83	+0.03	0.94
4. 71061,1	(1)	3.13	114.2	2.56	169.6	3.33	−0.25	0.81
	(2)	4.15	56.3	4.11	57.9	1.96	−0.03	0.85
5. 71501,1	(1)	3.75	74.3	3.60	82.5	2.24	−0.16	1.07
	(2)	3.95	64.7	3.94	65.1	1.84	−0.02	0.93
6. 72141,1	(1)	4.35	49.0	4.13	57.1	2.08	−0.18	0.97
	(2)	4.42	46.7	4.31	50.4	1.90	−0.11	0.92
7. 72141,15	(1)	4.40	47.4	4.30	50.8	2.12	−0.12	0.96
	(2)	4.41	47.0	4.45	45.8	1.87	+0.01	0.86
8. 72321,7	(1)	4.40	47.4	4.24	52.9	1.98	−0.16	1.01
	(2)	4.51	43.9	4.40	47.4	1.81	−0.11	0.94
9. 72441,7	(1)	4.18	55.2	3.94	65.1	2.25	−0.22	0.95
	(2)	4.38	48.0	4.23	53.3	1.86	−0.11	0.85
10. 72461,5	(1)	3.95	64.7	3.65	79.7	2.26	−0.26	0.91
	(2)	4.22	53.7	4.03	61.2	1.84	−0.18	0.83
11. 72501,1	(1)	4.07	59.5	3.90	67.0	2.26	−0.15	0.88
	(2)	4.27	51.8	4.14	56.7	1.99	−0.09	0.82
12. 72501,29	(1)	4.11	57.9	3.95	64.7	2.13	−0.17	0.94
	(2)	4.30	50.8	4.18	55.2	1.80	−0.10	0.81
13. 72701,29	(1)	4.17	55.6	4.02	61.6	2.12	−0.16	0.94
	(2)	4.30	50.8	4.20	54.4	1.87	−0.09	0.84
14. 73121,10	(1)	4.18	55.2	3.96	64.2	1.99	−0.19	0.85
	(2)	4.30	50.8	4.11	57.9	1.81	−0.15	0.81
15. 73141,4	(1)	3.81	71.3	3.49	89.0	2.44	−0.23	0.88
	(2)	4.20	54.4	3.99	62.9	1.93	−0.16	0.80
16. 73141,12	(1)	4.00	62.5	3.74	74.8	2.62	−0.19	0.92
	(2)	4.32	50.1	4.26	52.2	2.09	−0.06	0.81
17. 73221,1	(1)	3.82	70.8	3.39	95.4	2.66	−0.26	0.82
	(2)	4.29	49.0	3.96	64.2	2.20	−0.25	0.88
18. 73241,9	(1)	3.62	81.3	2.98	126.7	3.34	−0.28	0.84
	(2)	4.49	44.5	4.29	51.1	2.18	−0.12	0.88
19. 73261,1	(1)	4.00	62.5	3.53	86.6	2.70	−0.27	0.82
	(2)	4.52	43.6	4.17	55.6	2.16	−0.24	0.88
20. 73281,1	(1)	4.00	62.5	3.48	89.6	2.93	−0.31	0.97
	(2)	4.56	42.4	4.36	48.7	1.97	−0.14	0.79
21. 74001,2	(2)	4.53	43.3	4.47	45.1	1.63	−0.07	0.89
22. 74001,10	(2)	4.51	43.9	4.67	39.3	1.69	+0.10	0.91

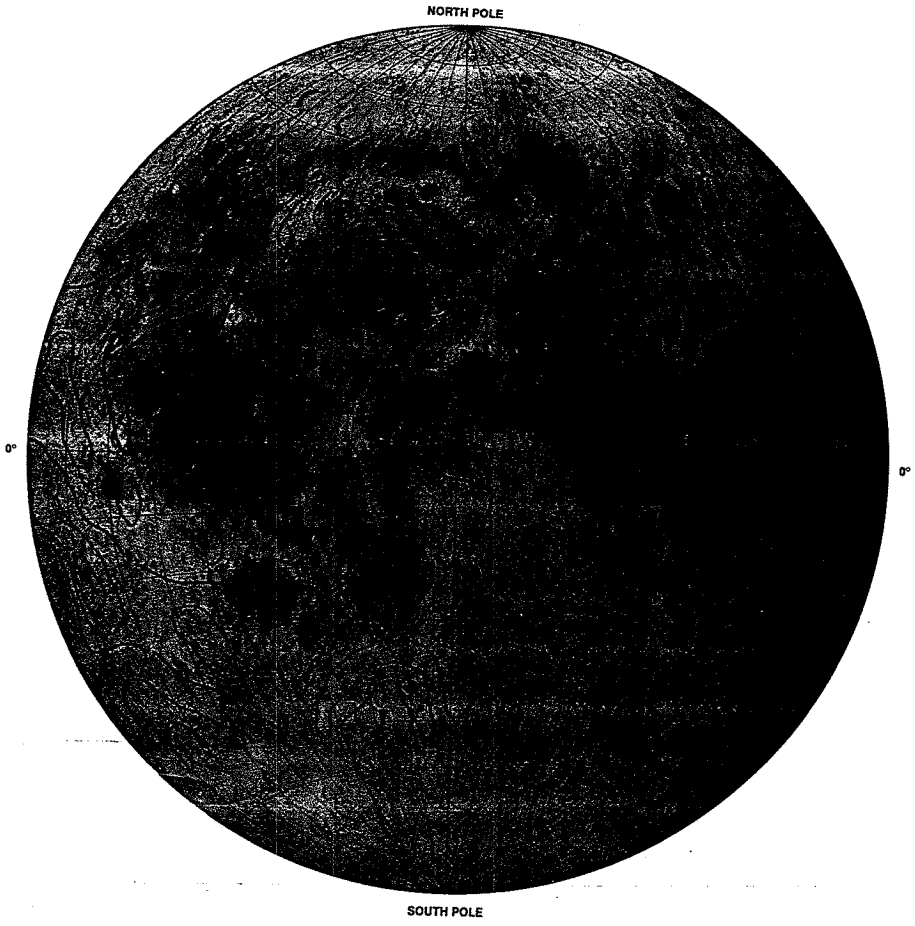

Fig. 10.7. Map of lunar nearside gravity field derived from radio tracking of the Lunar Orbiter 3, 4, and 5 spacecraft (*Müller and Sjogren,* 1968, 1969). Lunar north is at top. Contour interval is 20 milligals (mgal); supplemental 10-mgal contours (dashed lines) are shown for low-contrast regions. Closed contours around positive values indicate concentrations of excess mass (*mascons*), many of which are associated with the lunar maria. The largest mascon (+165 mgal) is associated with Mare Serenitatis; the second largest (+155 mgal) is associated with Mare Imbrium.

uplifted mantle material (*Wise and Yates,* 1970), to some combination of the two (*Bowin et al.,* 1975; *Phillips and Dvorak,* 1981).

10.3.2. Lunar Surface Magnetic Field

It was recognized early in lunar exploration that the Moon possesses at most a very weak internal magnetic field, and it is not yet clear that one exists at all. Surface magnetic measurements were performed by the surface magnetometers deployed at fixed locations at the Apollo 12, 15, and 16 sites. On the Apollo 14 and 16 missions, the astronauts used portable magnetometers to measure the magnetic fields along traverses within the landing area (*Dyal et al.,* 1974). These surface measurements found anomalous local areas with remanent magnetic fields as strong as 300 γ, or 0.24 A/m (a field strength that is still two orders of magnitude less than Earth's; see Table 3.1). Two subsatellites launched into lunar orbit from the Apollo 15 and 16 service modules carried magnetometers (*Coleman et al.,* 1972) to measure surface magnetism directly. These subsatellites also carried electron detectors that could indirectly determine smaller-scale surface magnetic fields by measuring the fluxes of electrons reflected from the lunar surface by magnetic anomalies (*Lin et al.,* 1976; Plate 10.6). The maximum signal detected at the subsatellite was about 0.0080 A/m (~10 γ), with a sensitivity of 0.0002 A/m (0.2 γ).

The measurements of reflected electrons by the subsatellites (*Lin et al.,* 1976) indicate that about 5% of the lunar maria surfaces have a significant magnetic field (i.e., detected by the subsatellites as a signal >0.0004 A/m, or >0.4 γ). These measurements also demonstrate that, in general, the lunar maria show relatively weak, bland surface fields, whereas the highlands display a diverse and heterogeneous field strength distribution. For reviews of the interpretations of lunar magnetic data, see *Fuller* (1974), *Dyal et al.* (1974), and *Hood et al.* (1979).

A major unresolved problem concerning lunar surface magnetism is the existence of localized strong magnetic anomalies detected from orbit (Plate 10.6), including those in the Reiner Gamma region (nearside) and near Van de Graaff Crater (farside). Several of these anomalies occur on the opposite sides of the Moon (antipodal) from young mare impact basins such as Imbrium and Crisium (*Hood,* 1987). The anomalies are often associated, especially at Reiner Gamma, with a peculiar pattern of light- and dark-colored swirls on the lunar surface.

These anomalies and swirls have generated speculation both during and since the Apollo program, and their origins have not yet been settled. Extralunar origins such as cometary impact or solar magnetic storms have been proposed, as well as lunar origins such as volcanism or alteration by gases from the lunar interior (*El-Baz,* 1972). Current hypotheses favor an origin resulting from magnetization of the regions antipodal to some of the major impacts on the Moon (*Lin et al.,* 1988; *Hood and Williams,* 1989). The origins of the swirls will probably not be resolved until these areas are actually mapped and sampled.

10.3.3. Radar Data for the Lunar Nearside

Radar-reflection data for the nearside of the Moon have been obtained using active Earth-based radio telescopes at both 3.8- and 70-cm wavelengths (*Zisk et al.,* 1974; *Thompson,* 1987). For any given radar measurement, two different images of the surface are generally produced (see section 9.3.2). In the region away from the *subradar point* (the point on the Moon in direct line from the radar source), the signal returned with the expected polarization sense (called the *polarized* component) produces an image of the lunar surface that appears similar to a surface illuminated by sunlight and includes highlights and shadows. In this case, however, the illumination is incident from the direction of the transmitter. A different signal, returned from the lunar surface with an opposite polarization sense (referred to as the *depolarized* component), is the result of surface scattering properties (i.e., roughness).

Radar-backscatter data for the lunar surface can be used to estimate the roughness of the surface on the scale of the wavelength (e.g., *Thompson et al.,* 1974). The intensity of radar backscatter is controlled chiefly by two sets of properties: the physical structure of the surface (i.e., amounts of blocks and craters) and the magnitude of the electromagnetic discontinuity at the surface, which is a function of the material properties (dielectric constant, loss tangent, and porosity) of the surface material. The major properties of radar-backscatter images are illustrated in the examples in Figs. 10.8–10.10. Fresh craters generally contain blocks and rubble that cause them to appear relatively rough at the scale of the radar wavelength, and they therefore appear bright in the backscatter images. A discussion of radar characteristics of lunar craters can be found in *Thompson et al.* (1974, 1979, 1980). The fine-grained regional pyroclastic (volcanic) deposits, such as the dark-mantle material sampled at the Apollo 17 site (see section 6.1.7), are generally smooth and produce very low radar backscatter. This characteristic is an important diagnostic property that allows major deposits of pyroclastic mantling material to be identified and mapped

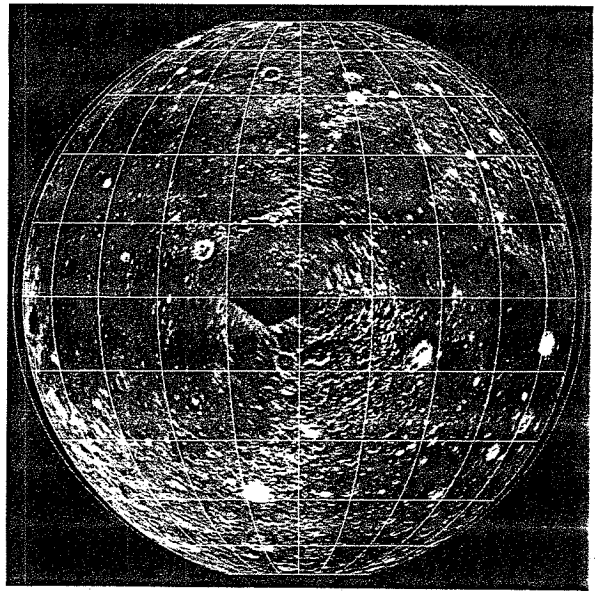

Fig. 10.8. Polarized radar-backscatter image of the nearside of the Moon, obtained during 1981–1984 with the 70-cm radar observatory at Arecibo, Puerto Rico (*Thompson*, 1987). Lunar north is at top. Since the width of the Arecibo radar antenna beam is only 10 arc-minutes (about one-third the width of the lunar disk as seen from Earth), this image is a calibrated mosaic constructed from 18 separate observations. The size of individual radar cells in the individual frames from which the image was made is 2–5 km. Dark areas correspond to individual maria with relatively smooth surfaces (e.g., Mare Crisium, on the right limb, along the first line of latitude above the equator). Bright splotches correspond to large young craters, which have blocky ejecta blankets and rays (e.g., Tycho, near the bottom center of the disk).

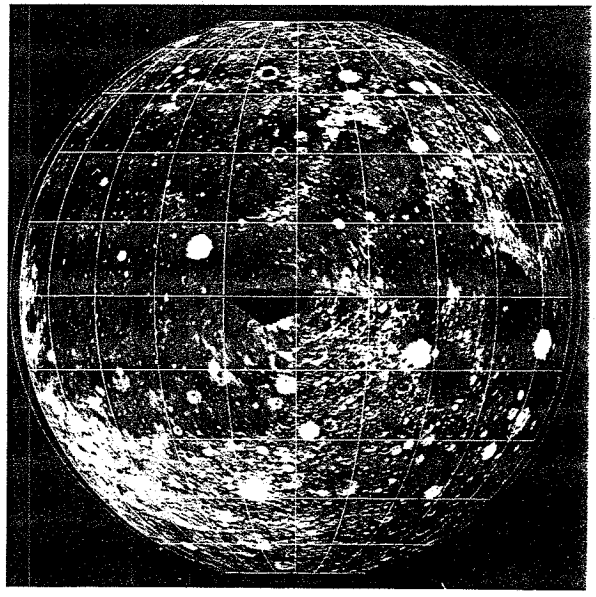

Fig. 10.9. Depolarized 70-cm radar backscatter calibrated image mosaic of the nearside of the Moon, obtained from the Arecibo radar data presented in Fig. 10.8. Lunar north is at top. In addition to high returns (bright areas) from the blocky ejecta surrounding large young craters, significant scattering differences can be observed regionally in the maria. For example, eastern Mare Tranquillitatis and western Oceanus Procellarum (center and left of lunar disk) have weaker return echoes than other maria, while the central portion of Mare Serenitatis and northern Mare Imbrium (upper center) have stronger echoes. In the highland areas on the nearside, areas near Mare Orientale (far left) have stronger echoes than do areas more distant from the Orientale Basin.

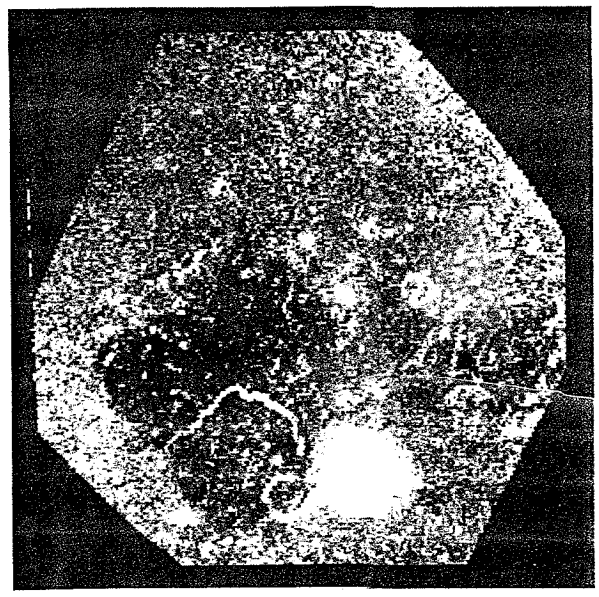

Fig. 10.10. Depolarized 3.8-cm radar backscatter image of the Aristarchus Plateau region of the Moon (ZAC reference area 6.26; *Zisk et al.*, 1974). Lunar north is at top. Radar cell size (equivalent to resolution) is about 3 km. This image provides good examples of the high backscatter from large, fresh lunar craters (bright areas), especially Aristarchus itself (large bright area at bottom), and also shows the exceptionally low backscatter from the pyroclastic deposits that cover much of the plateau (dark areas northwest of Aristarchus). The bright sinuous line west of Aristarchus is a rille (Schröter's Valley).

(*Pieters et al.*, 1973; *Gaddis et al.*, 1985). At longer wavelengths (tens of centimeters), the radar backscatter signal may in part be due to subsurface-volume scattering as well as surface-roughness scattering processes.

10.4. REGIONAL DISTRIBUTION OF LUNAR ROCK TYPES

Although coverage of the lunar surface by remotely-acquired geochemical data is limited, these data are adequate to demonstrate the compositional heterogeneity of the lunar surface. Plates 10.7–10.9 are preliminary maps showing the distribution of different rock types on the lunar surface as derived or inferred from the available remote measurements. From these data, it is clear that the Apollo and Luna collections of samples are not fully representative of the range of lunar materials exposed on the surface.

10.4.1. Mare Basalt Lavas

The compositions of lunar mare basalts from both sampled and unsampled regions of the Moon have been partially determined by using a combination of returned-sample analyses, orbital geochemical data, and Earth-based spectral reflectance measurements. The Al/Si ratios and the Fe data obtained by orbital X-ray and gamma-ray measurements made on the Apollo 15 and 16 missions (Plates 10.4 and 10.2) clearly indicate that the maria are mafic (low Al/Si and high Fe) and are clearly distinct from the more feldspathic (higher Al/Si and lower Fe) highlands. These data indicate that the fundamental basaltic nature of the maria extends beyond the Apollo and Luna sites and that essentially all the mare regions of the Moon are composed of basaltic lava flows.

The reflectance spectra of mature mare soils, measured by optical telescopes from Earth, provide independent geochemical information at a higher spatial resolution than provided by the orbital X-ray and gamma-ray data. The lateral extent of different mare basalt types on the nearside of the Moon has been mapped at moderately-high spatial resolution (a few kilometers) using data largely acquired with Earth-based telescopes. Multispectral images in the ultraviolet (UV), visible (VIS), and near-IR (0.95 μm) wavelengths, together with albedo images of the lunar nearside and a few hundred spectral reflectance measurements of small (10 km) mare regions, were the principal data used to identify and distinguish different basalt types on the Moon (see review in *Pieters*, 1978).